Discrete-dipole approximation for scattering by features on surfaces by means of a two-dimensional fast Fourier transform technique

Roland Schmehl,* Brent M. Nebeker, and E. Dan Hirleman

Department of Mechanical and Aerospace Engineering, Arizona State University, Tempe, Arizona 85287-6106

A two-dimensional fast Fourier transform technique is proposed for accelerating the computation of scattering characteristics of features on surfaces by using the discrete-dipole approximation. The two-dimensional fast Fourier transform reduces the CPU execution time dependence on the number of dipoles N from $O(N^2)$ to $O(N \log N)$. The capabilities and flexibility of a discrete-dipole code implementing the technique are demonstrated with scattering results from circuit features on surfaces. © 1997 Optical Society of America [S0740-3232(97)02311-9]

Key words: Light scattering, discrete-dipole approximation, coupled-dipole method, particles on surfaces, fast Fourier transform, differential scattering cross section, irradiance.

1. INTRODUCTION

Modeling of light scattering from features on surfaces is of interest in a variety of technical applications. In the semiconductor industry, submicrometer particle contaminants and defects on silicon wafers with circuit structures are detected and characterized by in-line scanning surface inspection systems. These systems use a focused laser beam to strike a surface and create a field of scattered light. The resulting scattered field is sampled and quantified with the use of one or more photodetectors, and surface defects and contaminants are detected. As design sizes of structures on silicon wafers continue to decrease, the importance of proper detection and characterization grows. The design of more sensitive inspection systems in the future will require a fundamental predictive capability for light scattering from such structures. A reliable model for predicting this light scattering would provide a flexible and efficient way to understand scattering processes.

Several models have recently been proposed to address the issue of light scattering. One basic model that has been used is based on the Lorenz–Mie theory, which takes into account surface interaction.[1,2] However, the Lorenz–Mie theory was developed for spherical features, and most contaminating features and circuit structures found on wafer surfaces are not spherical, so the Lorenz–Mie formulation may not predict scattering from the real features with acceptable accuracy. Another method developed uses the exact-image theory to model features above a perfect conductor.[3,4] Most substrates in the industry are not perfect conductors, and the features are confined to be spherical in this method, so other approaches need to be considered. Another approach is to apply the finite-element time-domain method to Maxwell's equations.[5,6] With this method, application of the boundary conditions sometimes can be difficult, and the computational requirements limit the feature sizes that

can be modeled. One of the most recent models developed is the discrete-source method, which entails the use of linear combinations of fields from dipoles and multipoles to solve Maxwell's equations and the boundary conditions.[7] Currently, however, this model is confined to features that are axisymmetric.

In this paper the method used to model the characteristics of light scattering from features on surfaces is the discrete-dipole approximation (DDA), also known as the coupled-dipole method. The DDA models the shape and composition of a feature as a set of dipoles on a lattice. An example of the dipoles used to model a sphere is shown in Fig. 1. An electric field induces a dipole moment at each dipole. The total electric field at each dipole includes contributions from the incident beam field, the field reflected from the surface, and the field created by interaction between the dipoles. Once the moment at each dipole is found, the scattered field outside the feature boundary can be determined. The DDA was originally developed to model particles in free space.[8–10] Taubenblatt and Tran[11] modified the method to model features on surfaces by employing the Sommerfeld integrals for interaction between dipoles and a surface.

Although developed heuristically by Purcell and Pennypacker,[8] the DDA method can be related to numerical methods that were developed from the Maxwell equations. Lakhtakia[12,13] provides a macroscopic view of the DDA method and relates the method to volume integral methods, which could include finite-element time-domain methods, as well as the method-of-moments technique. In the appendix of the paper by Hage and Greenberg,[14] a brief discussion is presented showing the relation between the electric field integral equation based on Maxwell's equations and the DDA method.

To model a scattering feature properly with the DDA method, the dipole spacing must be small compared with the electric field wavelength within the feature. This re-
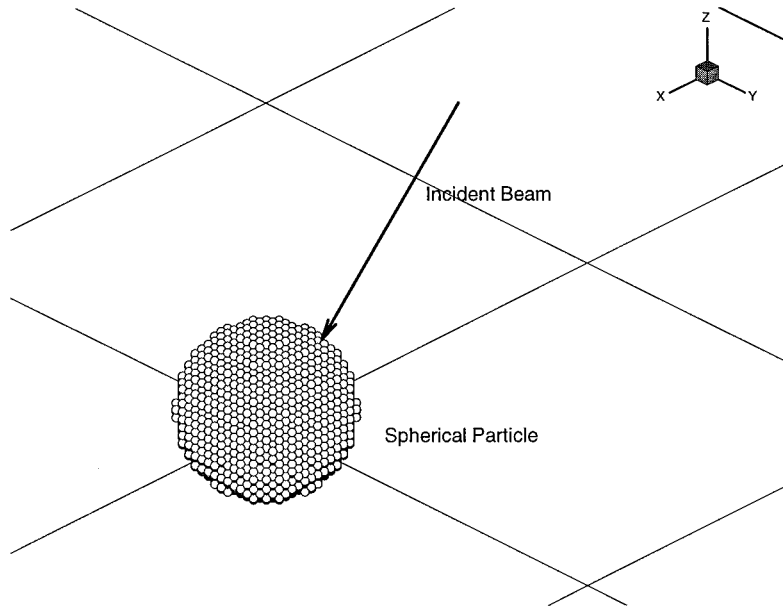
Fig. 1.   Dipole configuration for a spherical particle on a surface.

quirement can be represented by the relation $|m|kd \leq \beta$,[10] where d is the dipole lattice spacing, m is the refractive index, k is the wave number, and β is a parameter of the order 1. Thus there is a maximum lattice spacing allowable for a particular material, and the number of dipoles required to model a feature properly increases as its size increases. Also, a feature of higher refractive index will require more dipoles than a feature of the same size but lower refractive index. A common range used by investigators for dipole spacing as well as for element size when the finite-element methods are used is $\lambda/10$–$\lambda/20$, where λ is the wavelength of the incident beam.[15] The dipole lattice spacing also must be small enough to model the feature shape accurately. Hoekstra and Sloot[15] discuss the importance of dipole size with respect to feature shape.

Computational requirements increase significantly with the number of dipoles used to model a feature. Direct evaluation of the matrix equations developed by the DDA would require $O(N^2)$ operations, where N is the total number of dipoles used. This requirement becomes increasingly impractical as the number of dipoles increases. In this paper we discuss the application of the fast Fourier transform (FFT) technique to the DDA method to reduce the number of operations required. The FFT, introduced in 1965 by Cooley and Tukey,[16] can reduce the number of computational operations on N elements from $O(N^2)$ to $O(N \log N)$. Owing to this significant decrease in operations, the FFT has been a widely used analytic technique in fields such as optics,[17] electromagnetics,[18] and thermal analysis.[19] Goodman *et al.*[20] introduced the application of a three-dimensional fast Fourier transform (3-D FFT) to the DDA in modeling features in free space. This contribution significantly improved the usefulness of the DDA method in modeling features that require a large number of dipoles. The 3-D FFT technique requires periodicity within the dipole lattice in order to provide a computational advantage. When a feature is in free space, periodicity can be math-

ematically created in the three axis directions. However, when a surface is introduced, periodicity cannot be induced in the direction normal to the surface (z). In this paper we propose to apply a two-dimensional (2-D) FFT technique to the DDA method with surfaces, taking advantage of the periodicity in the directions parallel to the surface (x and y), though not in the z direction.

A code called DDSURF has been developed that is based on the DDSCAT code developed by Draine and Flatau,[10] with a modification to include surface interaction. DDSURF uses a 2-D FFT routine to solve for the dipole-moment distribution. In this paper we discuss the procedure taken to develop the application of the 2-D FFT technique to the DDA with surface interaction. The validity and flexibility of DDSURF will also be considered by comparison both with results found by experiment at Arizona State University and with computational predictions from other models.

2. METHOD
In the DDA method an array of dipoles is used to model features present on or near a surface. The feature shape is modeled by the placement of the dipoles, and the physical properties of the feature are modeled by designating the polarizability of each dipole. Figure 1 shows an example of the dipole configuration for a spherical particle on a surface.

A. Local Equations
When an electric field is applied to the array of dipoles, dipole moments are induced at each dipole. At the dipole i, the dipole moment $\mathbf{P}_i$ is related to the total electric field $\mathbf{E}_{\text{tot},i}$ by the dipole polarizability α_i through

$$\mathbf{P}_i = \alpha_i \mathbf{E}_{\text{tot},i}. \tag{1}$$

Recently, considerable effort has been made to model the polarizability for the DDA correctly. Several models are discussed by Draine and Goodman.[21] DDSURF has the

flexibility to use various models, but we have used the lattice dispersion relation as recommended.[21] This model is described in Eqs. (A1)–(A2e).

The total electric field at the dipole is the summation of the incident field, which includes the direct beam field and the beam field reflected from the surface; the field created by direct interaction between the dipoles; and the dipole fields reflected from the surface. The total electric field is represented as

$$\mathbf{E}_{\text{tot},i} = \mathbf{E}_{\text{inc},i} + \mathbf{E}_{\text{direct},i} + \mathbf{E}_{\text{reflected},i} . \qquad (2)$$

Substituting Eq. (2) into Eq. (1) we obtain an equation in terms of the three components of the total field:

$$(\alpha_i)^{-1}\mathbf{P}_i - \mathbf{E}_{\text{direct},i} - \mathbf{E}_{\text{reflected},i} = \mathbf{E}_{\text{inc},i} . \qquad (3)$$

The electric field by direct interaction between the dipoles, $\mathbf{E}_{\text{direct},i}$, can be represented as[22]

$$\mathbf{E}_{\text{direct},i} = \frac{k_0^2}{\epsilon_0} \sum_{j \neq i} \mathbf{G}_{ij} \cdot \mathbf{P}_j . \qquad (4)$$

The dyadic Green's function $\mathbf{G}_{ij}$ is defined in Eq. (A3).

The electric field interaction between dipoles with reflection from the surface, $\mathbf{E}_{\text{reflected},i}$, can be represented as[22]

$$\mathbf{E}_{\text{reflected},i} = \sum_{j=1}^{N} \left(\mathbf{S}_{ij} + \frac{k_2^2}{\epsilon_0} \frac{k_1^2 - k_2^2}{k_1^2 + k_2^2} \mathbf{G}_{ij}^I \right) \cdot \bar{P}_j . \qquad (5)$$

The components of the 3×3 $\mathbf{S}_{ij}$ matrix are given by the Sommerfeld integral terms in Eqs. (A7a)–(A7i). The Sommerfeld integral terms are computed numerically with routines developed by Lager and Lytle,[23] where k_1 and k_2 are the wave numbers for the feature and the surface, respectively, and ϵ_0 is the permittivity. The image dyadic Green's function is defined as[22]

$$\mathbf{G}_{ij}^I = -\mathbf{G}_{ij} \cdot \mathbf{I}_R , \qquad (6)$$

where $\mathbf{I}_R$ is the reflection dyad $\mathbf{I}_R = e_x e_x + e_y e_y - e_z e_z$. The dyadic product inverts the sign of the first two columns of the matrix of the dyadic Green's function but leaves the third column unchanged.

B. Global Equations

It is possible to represent the summation equations in terms of matrix equations consisting of N dipoles. The matrix equation for the entire problem can be represented as

$$(\mathbf{B} + \mathbf{A} + \mathbf{R})\mathbf{P} = \mathbf{E}_{\text{inc}} . \qquad (7)$$

For N total dipoles, $\mathbf{B}$ is the diagonal matrix of the inverse of the polarizabilities:

$$\mathbf{B} = \text{diag}(\alpha_{1x}^{-1}, \alpha_{1y}^{-1}, \alpha_{1z}^{-1}, ..., \alpha_{Nx}^{-1}, \alpha_{Ny}^{-1}, \alpha_{Nz}^{-1},), \qquad (8)$$

and $\mathbf{A}$ is the matrix that corresponds to Eq. (4), which is for direct interaction, and $\mathbf{R}$ is the matrix that corresponds to Eq. (5) for the reflected field interaction. $\mathbf{A}$ and $\mathbf{R}$ each consist of N^2 3×3 submatrices,

$$\mathbf{A} = \begin{bmatrix} \mathbf{A}_{11} & \cdots & \mathbf{A}_{1N} \\ \vdots & & \vdots \\ \mathbf{A}_{N1} & \cdots & \mathbf{A}_{NN} \end{bmatrix}, \quad \mathbf{R} = \begin{bmatrix} \mathbf{R}_{11} & \cdots & \mathbf{R}_{1N} \\ \vdots & & \vdots \\ \mathbf{R}_{N1} & \cdots & \mathbf{R}_{NN} \end{bmatrix},$$
$$(9)$$

where the submatrices are defined in Appendix A. $\mathbf{P}$ and $\mathbf{E}_{\text{inc}}$ are composed of N 1×3 vectors:

$$\mathbf{P} = (\mathbf{P}_1 ... \mathbf{P}_N)^T, \qquad \mathbf{E}_{\text{inc}} = (\mathbf{E}_{\text{inc},1} ... \mathbf{E}_{\text{inc},N})^T. \qquad (10)$$

C. Solution of the Matrix Equations

It is often necessary to use a large number of dipoles (>1000) to model features properly by the DDA method. Direct inversion of the ($\mathbf{B} + \mathbf{A} + \mathbf{R}$) matrix to solve Eq. (7) can prove to be impractical for large numbers of dipoles. Therefore iterative methods such as the complex-conjugate-gradient (CCG) method can be used for such large systems. DDSURF has the flexibility to use several different CCG methods, but we will use the method developed by Petravic and Kuo-Petravic[24] and used by Draine.[9] In the CCG method an initial guess for the polarization vector $\mathbf{P}^{(0)}$ is provided, and new estimates of $\mathbf{P}$ are made at every iteration. The CCG method requires only the matrix-vector products of $(\mathbf{B} + \mathbf{A} + \mathbf{R})\mathbf{P}^{(n)}$ and $(\mathbf{B} + \mathbf{A} + \mathbf{R})*\mathbf{P}^{(n)}$, where n indicates the iteration step and * indicates the Hermitian conjugate. Direct evaluation of these terms requires $O(N^2)$ operations. To reduce the excessive computational requirement from $O(N^2)$ to $O(N \log N)$, Goodman *et al.*[20] applied a 3-D FFT technique to the nonsurface DDA model. The FFT technique requires periodic conditions, and when a surface is present, it is not possible to have periodicity in the direction normal to the surface, z. We can, however, apply the FFT in the directions parallel to the surface plane, x and y. Thus we developed a 2-D FFT technique that is applied to the model for the case with a feature on a surface.

To apply the FFT in the x and y directions, we mathematically extend the original dipole lattice into a rectangular block, double the lattice size in the x and y directions, and induce periodicity. To maintain the proper physics of the problem, we force the dipole moments to zero at the lattice locations that lie outside the feature boundaries. Thus the induction of periodicity of the lattice does not limit the coverage of the DDA method when the FFT technique is used.

After the dipoles have been blocked and doubled in the x and y directions, we can show the steps to be taken to apply the FFT to the direct-interaction electric field component and the reflection-interaction electric field component. The direct-interaction electric field at each dipole can be determined by summing contributions from each dipole:

$$\mathbf{E}_{\text{direct},i} = \sum_{j_z=1}^{N} \left(\sum_{j_y=1}^{2N_y} \sum_{j_x=1}^{2N_x} \mathbf{A}_{ij}\mathbf{P}_j \right), \qquad (11)$$

where N_x, N_y, and N_z are the original number of dipoles in the x, y, and z directions, respectively.

The elements of $\mathbf{A}_{ij}$ are dependent only on the distance vector $\mathbf{r}_{ij} = \mathbf{r}_i - \mathbf{r}_j$ between dipole i and dipole j, and thus we can define

$$\mathbf{A}'_{i-j} \equiv \begin{cases} 0 & \text{for } i = j \\ \mathbf{A}_{ij} & \text{for } i \neq j \end{cases}, \qquad (12)$$

and Eq. (11) can be now written in the form of a convolution:

$$\mathbf{E}_{\mathrm{direct},i} = \sum_{j_z=1}^{N_z} \left(\sum_{j_y=1}^{2N_y} \sum_{j_x=1}^{2N_x} \mathbf{A}'_{i-j} \mathbf{P}_j \right). \quad (13)$$

Since Eq. (13) is a convolution, and if we take the Fourier transform in the x and y directions, keeping the z dependency in the original domain, we obtain the summation in the z direction:

$$\hat{\mathbf{E}}_{\mathrm{direct},(n_x,n_y,i_z)} = \sum_{j_z=1}^{N_z} \hat{\mathbf{A}}_{(n_x,n_y,i_z-j_z)} \hat{\mathbf{P}}_{(n_x,n_y,j_z)}, \quad (14)$$

where the caret denotes the Fourier transform.

Similar steps can be taken for the reflection-interaction component of the total electric field. For the reflection-interaction terms, we can think of the interaction between the actual dipole above the surface and a corresponding image dipole below the surface, j:

$$\mathbf{E}_{\mathrm{reflected},i} = \sum_{j_z=1}^{N_z} \left(\sum_{j_y=1}^{2N_y} \sum_{j_x=1}^{2N_x} \mathbf{R}_{ij} \mathbf{P}_j \right). \quad (15)$$

The elements of $\mathbf{R}$ are dependent only on the distance vectors between the dipoles at i and the image dipoles at j, $\mathbf{r}_{ij} = \mathbf{r}_i - \mathbf{r}_j$, and thus we can define

$$\mathbf{R}'_{i-j} \equiv \mathbf{R}_{ij} \qquad \text{for all } i, j, \quad (16)$$

and Eq. (15) can be now written as a convolution:

$$\mathbf{E}_{\mathrm{reflected},i} = \sum_{j_z=1}^{N_z} \left(\sum_{j_y=1}^{2N_y} \sum_{j_x=1}^{2N_x} \mathbf{R}'_{i-j} \mathbf{P}_j \right). \quad (17)$$

By the linearity property of Fourier transforms, we can apply the convolution theorem in the j_x and j_y indices and thereby represent Eq. (17) in Fourier representation as

$$\hat{\mathbf{E}}_{\mathrm{reflected},(n_x,n_y,i_z)} = \sum_{j_z=1}^{N_z} \hat{\mathbf{R}}'_{(n_x,n_y,i_z+j_z)} \hat{\mathbf{P}}_{(n_x,n_y,j_z)}. \quad (18)$$

Thus Eqs. (14) and (18) can be combined to create the transformed equation that relates the incident electric field and the dipole-moment distribution:

$$\hat{\mathbf{Y}}_{(n_x,n_y,i_z)} = \sum_{j_z=1}^{N_z} (\hat{\mathbf{A}}'_{(n_x,n_y,i_z-j_z)} + \hat{\mathbf{R}}'_{(n_x,n_y,i_z+j_z)}) \hat{\mathbf{P}}_{(n_x,n_y,j_z)}, \quad (19)$$

and for the Hermitian form,

$$\hat{\mathbf{Y}}^*_{(n_x,n_y,i_z)} = \sum_{j_z=1}^{N_z} (\hat{\mathbf{A}}'_{(n_x,n_y,i_z-j_z)}$$
$$+ \hat{\mathbf{R}}'_{(n_x,n_y,i_z+j_z)})^* \hat{\mathbf{P}}_{(n_x,n_y,j_z)}. \quad (20)$$

The FFT routine used in DDSURF was developed by Brenner.[25] Depending on at what point DDSURF is in the CCG algorithm, the inverse Fourier transform is taken of either $\hat{\mathbf{Y}}_{(n_x,n_y,i_z)}$ or $\hat{\mathbf{Y}}^*_{(n_x,n_y,i_z)}$ and is combined with the product of the polarizability diagonal matrix $\mathbf{B}$ and the most recent estimate of the polarization matrix $\mathbf{P}$. Since $\mathbf{P}$ has $3N$ elements, the code should in theory converge in $3N$ iterations. Draine and Flatau[10] state that 10–100 iterations are often sufficient to find solutions with high accuracy.

D. Far-Zone Approximation

Once the dipole-moment distribution has been determined, the scattering parameters can be found. To find the angle-resolved scattering pattern, we need to determine the electric field in the far zone. A postprocessor code called RDSURF was developed to compute the far field from the dipole-moment distribution within the feature. From the feature to the receiving detector there are two scattering components to consider. One component is produced by direct scattering from each dipole, and the other component reaches the detector after reflection off the surface. The latter component is found by using the Fresnel equations. The total electric field at a receiving point can be represented as[22]

$$\mathbf{E}_{\mathrm{sca}}(r) = k_0{}^2 \frac{\exp(ik_0 r)}{4\pi r} \sum_{j=1}^{N} \{\exp(-ik_{\mathrm{sca}} r_j)[(\mathbf{P}_j \cdot \hat{e}_1)\hat{e}_1$$
$$+ (\mathbf{P}_1 \cdot \hat{e}_2)\hat{e}_2] + \exp(-ik_{I,\mathrm{sca}} r_j)$$
$$\times [R^{\mathrm{TM}}(\mathbf{P}_j \cdot \hat{e}_1)\hat{e}_1 + R^{\mathrm{TE}}(\mathbf{P}_j \cdot \hat{e}_2)\hat{e}_2]\}, \quad (21)$$

and the irradiance can be found by multiplying the scattered E field by its complex conjugate:

$$I_{\mathrm{sca}} = \mathbf{E}_{\mathrm{sca}} \mathbf{E}_{\mathrm{sca}}^-. \quad (22)$$

E. Computed Parameters

At Arizona State University, experimental results for scattering from the features on surfaces are collected in the form of a differential scattering cross section, $dC_{\mathrm{sca}}/d\Omega$. Differential scattering cross section is defined as the energy scattered per unit time per unit solid angle about a certain direction. Bohren and Huffman[26] derived an expression for this:

$$\frac{dC_{\mathrm{sca}}}{d\Omega} = \lim_{\Omega \to 0} \left(\frac{C_{\mathrm{sca}}}{\Omega} \right) \approx \frac{I_{\mathrm{sca}} A}{I_{\mathrm{inc}}(A/r^2)} = \frac{r^2 I_{\mathrm{sca}}}{I_{\mathrm{inc}}}, \quad (23)$$

where I_{sca} is the scattered irradiance, A is the detection area, r is the distance from the feature to the observation point, I_{inc} is the incident irradiance, and Ω is the detection solid angle.

3. CALCULATIONS AND RESULTS

A. Fast Fourier Transform

Figure 2 demonstrates the effect of 2-D FFT implementation on the CPU time requirements for an IBM 370 RS6000 workstation. The cases considered were for a cubical feature on a surface and a spherical feature on a surface. Table 1 shows the number of dipoles and the corresponding CPU time-per-iteration requirements for the FFT and non-FFT methods for the spherical-feature case. When the FFT is not used, it is not necessary to extend the dipole lattice to form a rectangular shape, and thus CPU time per iteration varies with shape only when the FFT is used. However, using the FFT significantly reduces the time requirement for every case considered, even when the symmetry requirements force usage of a much greater number of dipoles.
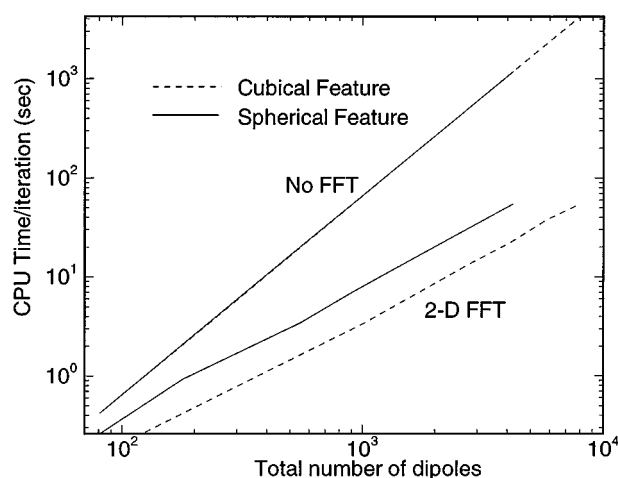
Fig. 2. Comparison of required CPU time per iteration for DDSURF with and without the 2-D FFT. Computations were performed on an IBM 370 RS6000 workstation.

Table 1. Number of Dipoles Needed and CPU Time per Iteration for a Spherical Particle on a Surface, with FFT and non-FFT Routines

# Dipoles/ Sphere (Active)	# Dipoles, Total (FFT)/(no FFT)	CPU Time (FFT) (seconds per iteration)	CPU Time (no FFT) (seconds per iteration)
81	125/81	0.26	0.42
179	343/179	0.93	2.10
552	1000/552	3.36	20.1
912	1728/912	7.04	55.0
4224	8000/4224	54.6	1180

[a] CPU times are for an IBM 370 RS6000 workstation.

B. Comparisons with Other Models

Figure 3 shows results of calculations for a scattering parameter determined by DDSURF, the DDA code developed by Taubenblatt and Tran,[11] and the finite-element method developed by Wojcik *et al.*,[5] which is based on Maxwell's equations. The parameter in Fig. 3 is the same as the one used in Fig. 4 of Taubenblatt and Tran.[11] The parameter is the ratio of the scattered and the incident beam irradiance multiplied by $k^2 r^2$, where $k = 2\pi/\lambda$ and r is the radius of the feature. DDSURF agrees well with the Taubenblatt code over most scattering angles, showing a maximum discrepancy of 19% at 59° near the first scattering minimum. However, at the first minimum the values determined by DDSURF show agreement within 5% with the Wojcik finite-element-method results.

C. Comparisons with Experiment

We also compared results from DDSURF with experimental results found at Arizona State University. A scatterometer arrangement that is used to determine scattering characteristics from small features on surfaces is shown in Fig. 4. Scattering from a feature or structure on a silicon surface is created by a focused laser beam. For the cases considered in this paper, the incident beam has a wavelength of 632.8 nm and strikes the substrate at a 45°

angle measured from the surface normal. The differential scattering cross section is measured by the scatterometer.

The scattered-irradiance signature pattern is sampled experimentally by a ring/wedge photodetector. Figure 5 shows the geometry and position of the detector with respect to the feature on the surface. The differential scattering cross section for the cases considered here are measured in the ring and wedge regions of the photodetector. The ring region consists of 32 concentric ring detectors at angles from 0.6° to 62.7° from the specular direction, which is 45° from the surface-normal vector. The wedge region consists of 32 wedge detectors that range from −90° to 90° from the center in the ϕ direction. The center of the detector is 8.2 mm from the sample feature. The differently shaped detectors permit the determination of different characteristics resulting from the scattered light. The ring region provides information about the size of the scattering feature, and the wedge section provides information about the configuration of the feature.

The postprocessor RDSURF modeled the ring and wedge regions of the detector, and $dC_{sca}/d\Omega$ at each ring and wedge was found by averaging the differential scattering cross section at a large number of discrete points within each detector.

1. Scattering from a Spherical Particle

We now discuss scattering from a spherical particle on a flat surface. Scattering experiments were conducted for a 0.482-μm polystyrene latex (PSL) sphere on a silicon substrate. An s-polarized 632.8-nm beam was incident on the sphere at 45° from the surface normal. Figure 1 displays the dipole configuration for a spherical particle on a surface. We first show the intensity distribution of the scattered light from the sphere. Figure 6 shows the plane of detection where the ring/wedge detector lies, and Fig. 7 shows the calculated intensity distribution of the scattered beam on a logarithmic scale. To quantify the scattering results and to compare them with experiment, Figs. 8(a) and 8(b) show the numerical predictions and
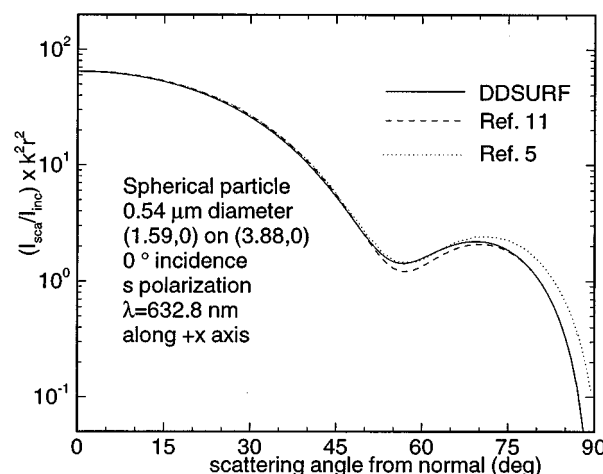

Fig. 3. Prediction of scattering in the $x-z$ plane as a function of the angle measured from the surface normal by DDSURF compared with predictions by Taubenblatt and Tran[11] and Wojcik *et al.*[5]
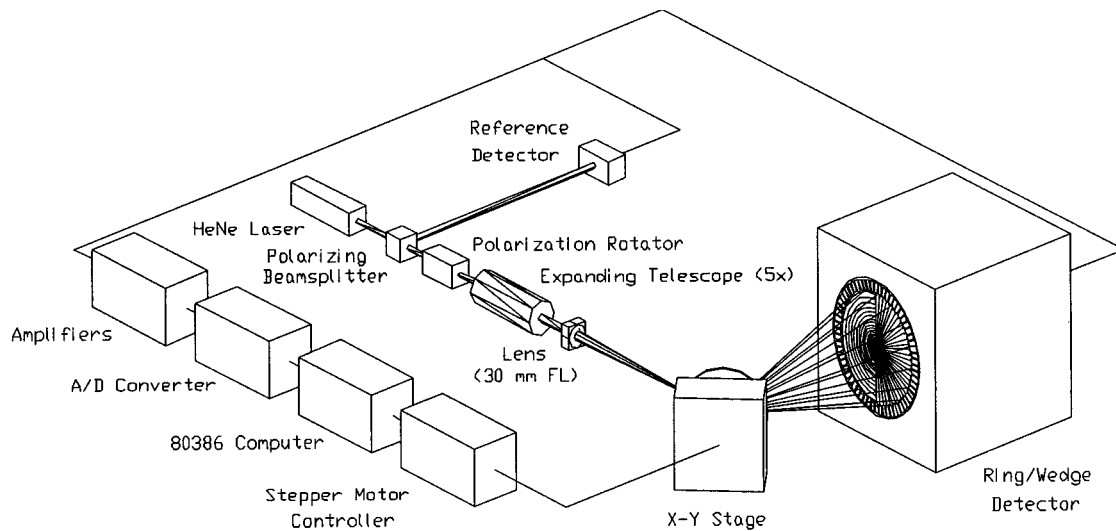
Fig. 4. Arizona State University scatterometer used for measuring light scatter from samples.
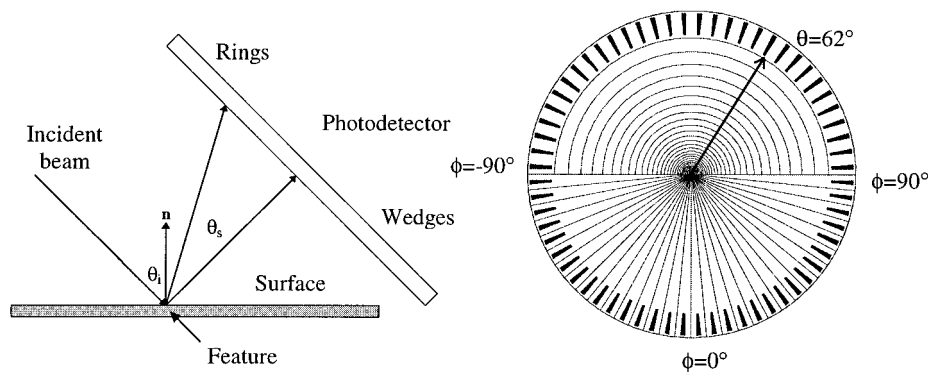

Fig. 5. Configuration of the ring/wedge photodetector used to measure light scatter.

the experimental results for the differential scattering cross section computed from the ring and the wedge regions of the photodetector, respectively. Because of optical noise, the comparisons between the experiment and the numerical predictions in Fig. 8(a) started at the tenth ring from the center. We see that the DDSURF results and the experimental results are in relatively good agreement. For the ring region the predictions were between 5% and 60% higher, and the results for the wedge region show agreement within 50%. Several factors could account for the differences between experiment and the numerical results. We can see that in Fig. 7, since the scattering feature is spherical, the scattered light is symmetrical about the aximuthal axis. We would therefore expect the wedge data to be symmetrical about the 0° angle. By examination of the experimental results in Fig. 8(b), we can deduce that the photodetector was not aligned perpendicular to the plane of incidence. We see that the experimental results are slightly asymmetric, whereas the computed results are symmetric. Other differences could be the result of variation of the sphere diameter from the 0.482 μm as specified by the manufacturer and the result of an oxide layer that may be present on the silicon substrate because of exposure to the environment. Experimental uncertainties such as beam
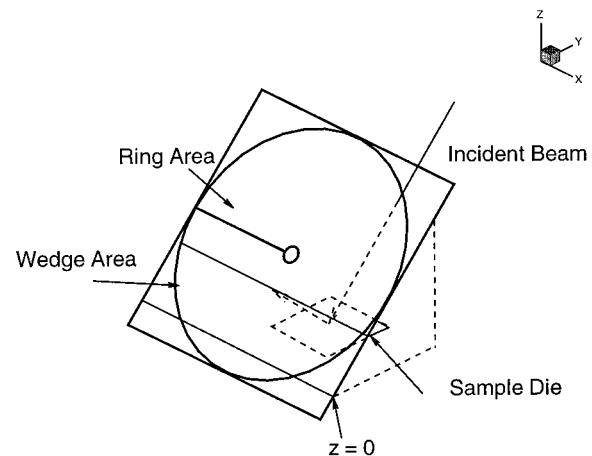

Fig. 6. Plane of detection for the ring/wedge photodetector with respect to the sample die.

power, beam width, and detector distance can also account for the difference between experiment and prediction.

2. Scattering from Nonspherical Features
Investigating scattering from a fundamental particle shape such as a sphere is important; however, the primary objective for developing DDSURF is to model scatter-
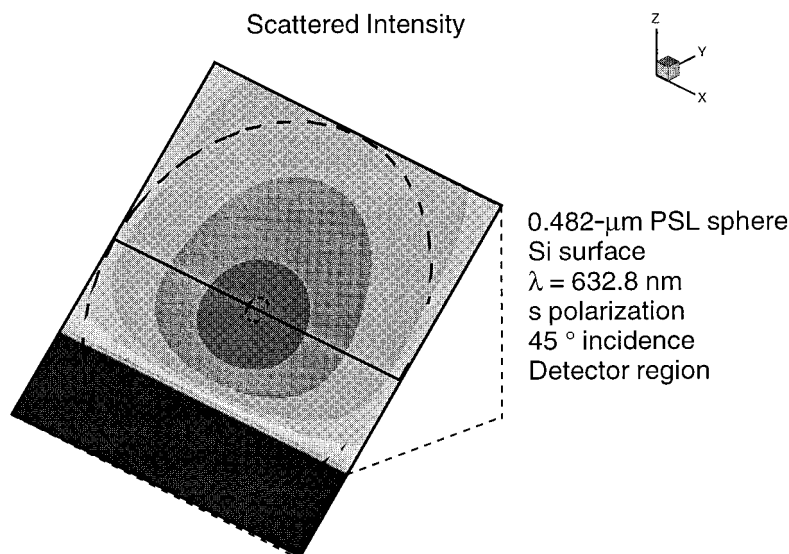
Scattered Intensity

0.482-μm PSL sphere
Si surface
λ = 632.8 nm
s polarization
45 ° incidence
Detector region

Fig. 7.   Predicted intensity distribution of light scattered from a 0.482-μm PSL sphere on a Si surface.
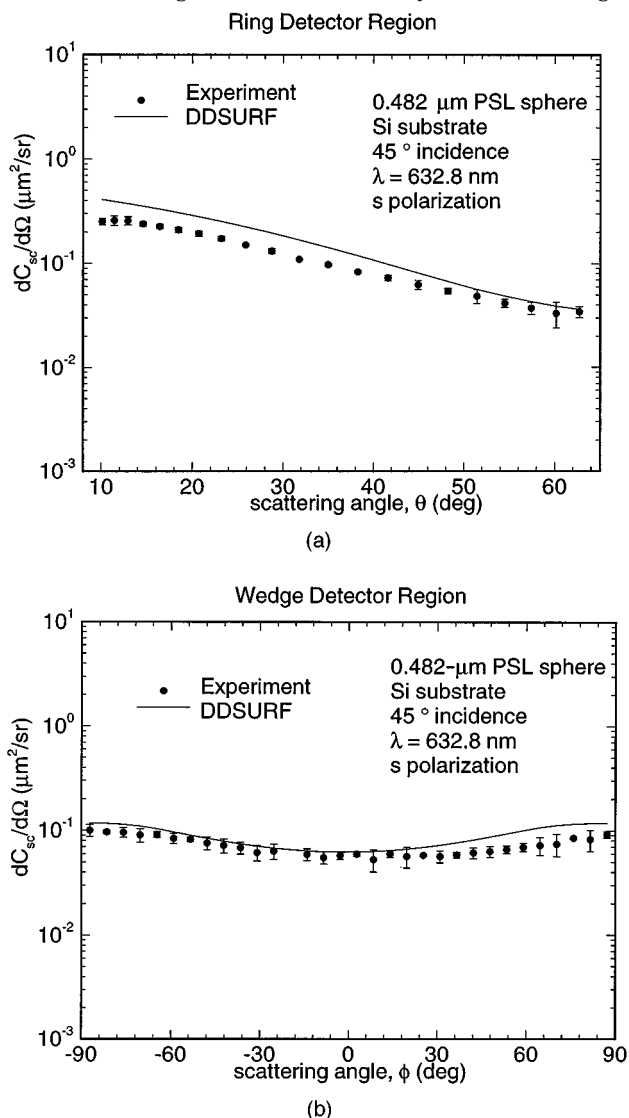

(a)

(b)

Fig. 8.   Numerical predictions and experimental calculations of the differential scattering cross sections for (a) the ring region and (b) the wedge region of the ring/wedge photodetector for a 0.482-μm PSL sphere on a Si surface.

ing from a wide range of feature configurations that are of interest to the silicon wafer industry. These features are integrated circuits on silicon wafers. At Arizona State University, light-scattering experiments have been conducted on SiO_2 features on the ASU/SRC section of the silicon SEMATECH Standard Wafer Defect Die developed by VLSI Standards Inc.[27] The features on the defect die were developed to represent the basic geometry of integrated circuits. Figure 9 shows a configuration of a cornered feature that was investigated on the defect die. A spherical PSL contaminant was placed near the feature to simulate contamination that is sometimes found during manufacturing. Investigation of the effect of the contaminant particle on the scattering from the die allows the user of the code to detect the presence of the contaminant.

Figure 10 shows the scattered-light pattern from the cornered-feature–contaminant configuration determined by DDSURF. The presence of the cornered feature and the scattering interaction between the contaminant and the feature cause the light-scattering pattern to be significantly more complicated than the pattern for the sphere only as seen in Fig. 7. Because of this complicated nature, it is important to be able to quantify the scattering by using the ring/wedge detector.

Figures 11(a) and 11(b) show the experimentally and numerically determined differential scattering cross sections for scattering in the ring and the wedge regions, respectively, of the ASU ring/wedge detector. In Fig. 11(a) we see that there is excellent agreement between experiment and numerical results. The comparisons for this configuration are better than the comparisons for the sphere-only configuration. In Fig. 11(b) we can clearly detect the presence of the particle contaminant, with the hump region at scattering angles near 20°. The differential scattering cross sections predicted by DDSURF follow this experimental trend very closely. The numerical results are consistently lower than in the experiment for the wedge region. As mentioned above, this may be due to experimental uncertainty. However, DDSURF has shown the ability to follow the trends of the experiment

extremely well, and this can be useful to the developers of particle-detection systems in the silicon industry. Experimental and numerical computations of other feature–contaminant configurations will be discussed in a future paper.

4. SUMMARY

The DDA method can be used to determine scattering characteristics of features on surfaces. A major challenge to the use of the DDA method is the computational power needed to solve the matrix equations. The 2-D FFT method developed here reduces the computational requirements from $O(N^2)$ to $O(N \log N)$ per iteration, al-

lowing for a larger range of features in terms of size and refractive index that can be practically considered here. The DDA code created to implement the 2-D FFT (DD-SURF) has been used in a series of comparisons with other models and with experimental results. DDSURF agrees well with other DDA methods that have been developed and with a finite-element method considered. DDSURF also exhibits the ability to predict scattering from non-spherical features on surfaces.

APPENDIX A

1. Polarizability
The relation for calculating the polarizability by means of the lattice dispersion relation method[21] is

$$\alpha_i = \frac{\alpha_i^{(0)}}{1 + (\alpha^{(0)}/d^3)[(b_1 + m^2 b_2 + m^2 b_3 S)(k_0 d)^2 - (2/3)i(k_0 d)^3]}, \quad \text{(A1)}$$
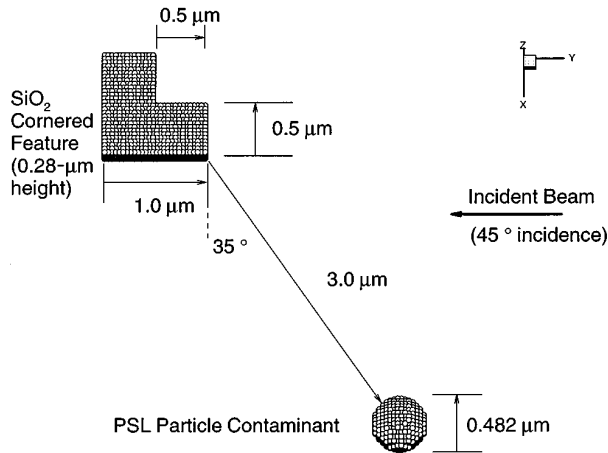
where

$$\alpha_j^{(0)} = 3 \epsilon_0 \frac{m_j^2 - 1}{m_j^2 + 2} \Delta V_j, \quad \text{(A2a)}$$

$$b_1 = -1.8915316, \quad \text{(A2b)}$$

$$b_2 = 0.1648469, \quad \text{(A2c)}$$

$$b_3 = -1.7700004, \quad \text{(A2d)}$$

$$S \equiv \sum_j (a_j e_j^{(0)})^2, \quad \text{(A2e)}$$

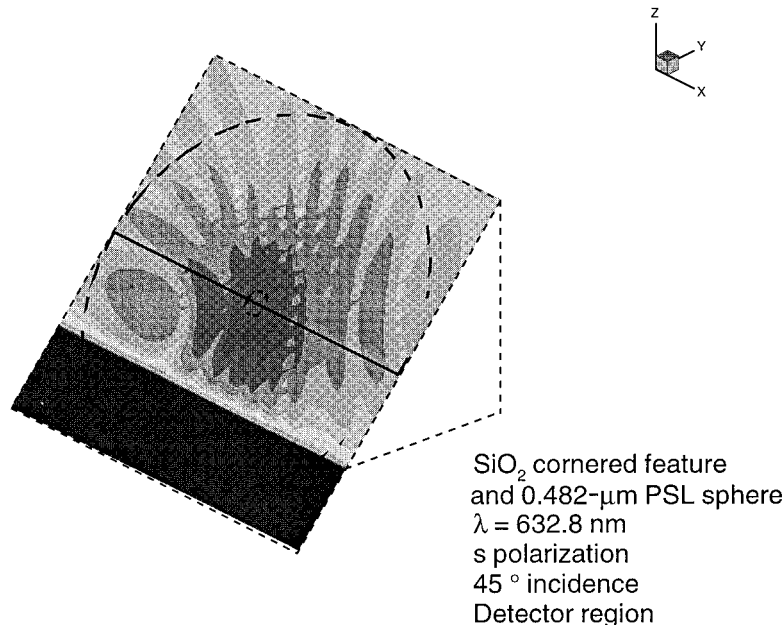a_j is the unit propagation vector, $e_j^{(0)}$ is the unit polarization vector, and d is the dipole spacing.

Fig. 9.   Dipole arrangement for cornered-feature–contaminant configuration.

Fig. 10.   Predicted intensity distribution of light scattered from a SiO_2 cornered-feature–PSL sphere contaminant configuration on a Si surface.
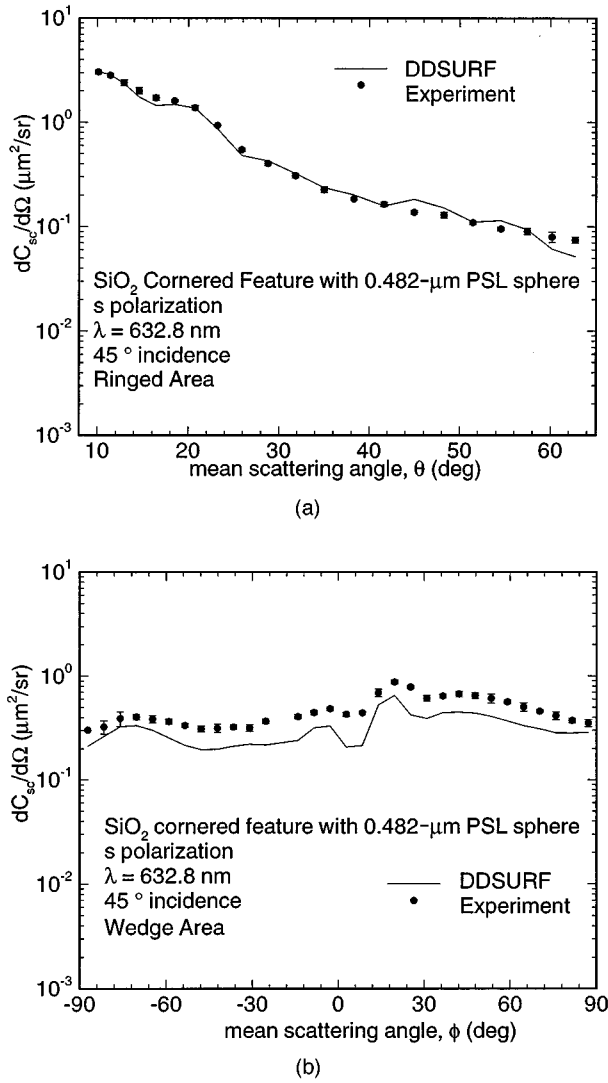
(a)

(b)

Fig. 11. Numerical predictions and experimental calculations of the differential scattering cross sections for (a) the ring region and (b) the wedge region of the ring/wedge photodetector for a SiO$_2$ cornered-feature–PSL sphere contaminant configuration on a Si surface.

2. Dyadic Green's Function

The dyadic Green's function can be represented in the form[28]

$$\mathbf{G}(\mathbf{R}) = (\mathbf{I} - \hat{R}\hat{R})g(\mathbf{R}) + \frac{i}{kR}(\mathbf{I} - 3\hat{R}\hat{R})g(\mathbf{R})$$

$$- \frac{1}{k^2R^2}(\mathbf{I} - 3\hat{R}\hat{R})g(\mathbf{R}), \tag{A3}$$

where we introduce

$$\mathbf{R} = \mathbf{r} - \mathbf{r}', \tag{A4a}$$

$$R = |\mathbf{r} - \mathbf{r}'|, \tag{A4b}$$

$$\hat{R} = \mathbf{R}/R, \tag{A4c}$$

$$g(\mathbf{R}) = (4\pi R)^{-1}\exp(ikR). \tag{A4d}$$

The geometric representation of these variables can be found in Fig. 12. The first term in Eq. (A3) varies as $1/R$ and can be referred to as the radiation term; it dominates at distances that are far from the source. The second term varies as $1/R^2$ and can be referred to as the induction term; it dominates at intermediate distances. The third term varies as $1/R^3$; it dominates close to the source and can be called the electrostatic term.[28]

3. Direct-Interaction Matrix

As stated earlier in the paper, **A** is the interaction matrix that considers the direct interaction between the dipoles. The components of each submatrix in **A** are the following:

For the diagonal submatrices,

$$\mathbf{A}_{ii} = \begin{bmatrix} 0 & 0 & 0 \\ 0 & 0 & 0 \\ 0 & 0 & 0 \end{bmatrix}. \tag{A5a}$$

For the off-diagonal submatrices,

$$\mathbf{A}_{ij} = C_{ij} \begin{bmatrix} \beta_{ij} + \gamma_{ij}\hat{r}_{ij,x}^2 & \gamma_{ij}\hat{r}_{ij,x}\hat{r}_{ij,y} & \gamma_{ij}\hat{r}_{ij,x}\hat{r}_{ij,z} \\ \gamma_{ij}\hat{r}_{ij,y}\hat{r}_{ij,x} & \beta_{ij} + \gamma_{ij}\hat{r}_{j,y}^2 & \gamma_{ij}\hat{r}_{ij,y}\hat{r}_{ij,z} \\ \gamma_{ij}\hat{r}_{ij,z}\hat{r}_{ij,x} & \gamma_{ij}\hat{r}_{ij,z}\hat{r}_{ij,y} & \beta_{ij} + \gamma_{ij}\hat{r}_{ij,z}^2 \end{bmatrix}, \tag{A5b}$$

where

$$\hat{r}_{ij,x} = \frac{r_{ij,x}}{r_{ij}}, \qquad \hat{r}_{ij,y} = \frac{r_{ij,y}}{r_{ij}}, \qquad \hat{r}_{ij,z} = \frac{r_{ij,z}}{r_{ij}}, \tag{A6a}$$

$$C_{ij} = -\frac{k_0^2}{4\pi\epsilon_0}\exp(ik_0r_{ij})(r_{ij})^{-1}, \tag{A6b}$$

$$\beta_{ij} = [1 - (k_0r_{ij})^{-2} + i(k_0r_{ij})^{-1}], \tag{A6c}$$

$$\gamma_{ij} = -[1 - 3(k_0r_{ij})^{-2} + 3(k_0r_{ij})^{-1}i], \tag{A6d}$$

$$r_{ij} = [(x_i - x_r)^2 + (y_i - y_j)^2 + (z_i - z_j)^2]^{1/2}. \tag{A6e}$$

4. Sommerfeld Integrals/Reflection Interaction

The components of the reflection interaction submatrix, $\mathbf{R}_{ij}$, can be found by considering the equations for the dipole reflection E field. The following are equations for
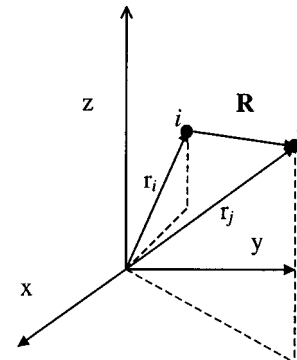

Fig. 12. Geometry of two dipoles and the terms referred to in the Green's function in Eq. (A3).

the E field over a dielectric surface, which will include the Sommerfeld integrals: I_ρ^V, I_z^V, I_ϕ^H, I_ρ^H.[22]

P_x dipole,

$$E_x^{(x)} = C\left\{\left[\left[\left(\frac{x}{\rho}\right)^2 I_\rho^H - \left(\frac{y}{\rho}\right)^2 I_\phi^H\right] - \frac{k_1^2 - k_2^2}{k_1^2 + k_2^2}\right.\right.$$
$$\left.\left.\times\left[\left(\frac{\partial^2}{\partial x^2} + k_2^2\right)4\pi g_I\right]\right\}P_x, \quad\quad (A7a)$$

$$E_z^{(z)} = C\left\{I_z^V + \frac{k_1^2 - k_2^2}{k_1^2 + k_2^2}\right.$$
$$\left.\times\left[\left(\frac{\partial^2}{\partial z^2} + k_2^2\right)4\pi g_I\right]\right\}P_z, \quad\quad (A7i)$$

where $C = (4\pi\epsilon_0)^{-1}$.

Equations (A7a)–(A7i) can be used to find the components for the $\mathbf{R}_{ij}$ submatrices:

$$\mathbf{R}_{ij} = -(4\pi\epsilon_0)^{-1}\begin{bmatrix} \hat{r}_{I,ij,x}^2 I_\rho^H - \hat{r}_{I,ij,y}^2 I_\phi^H & \hat{r}_{I,ij,x}\hat{r}_{I,ij,y}[I_\rho^H + I_\phi^H] & \hat{r}_{I,ij,x}I_\rho^V \\ \hat{r}_{I,ij,x}\hat{r}_{I,ij,y}[I_\rho^H + I_\phi^H] & \hat{r}_{I,ij,y}^2 I_\rho^H - \hat{r}_{I,ij,x}^2 I_\phi^H & \hat{r}_{I,ij,y}I_\rho^V \\ -\hat{r}_{I,ij,x}I_\rho^V & -\hat{r}_{I,ij,y}I_\rho^V & I_z^V \end{bmatrix}$$
$$- \frac{k_1^2 - k_2^2}{k_1^2 + k_2^2}\frac{\exp(ik_0 r_{I,ij})}{4\pi\epsilon_0 r_{I,ij}}\begin{bmatrix} -(\beta_{I,ij} + \gamma_{I,ij}\hat{r}_{I,ij,x}^2) & -(\gamma_{I,ij}\hat{r}_{I,ij,x}\hat{r}_{I,ij,y}) & \gamma_{I,ij}\hat{r}_{I,ij,x}\hat{r}_{I,ij,z} \\ -(\gamma_{I,ij}\hat{r}_{I,ij,y}\hat{r}_{I,ij,x}) & -(\beta_{I,ij} + \gamma_{I,ij}\hat{r}_{I,ij,y}^2) & \gamma_{I,ij}\hat{r}_{I,ij,y}\hat{r}_{I,ij,z} \\ -(\gamma_{I,ij}\hat{r}_{I,ij,z}\hat{r}_{I,ij,x}) & -(\gamma_{I,ij}\hat{r}_{I,ij,z}\hat{r}_{I,ij,y}) & \beta_{I,ij} + \gamma_{I,ij}\hat{r}_{I,ij,z}^2 \end{bmatrix}, \quad (A8)$$

$$E_y^{(x)} = C\left[\frac{xy}{\rho^2}(I_\rho^H + I_\phi^H) - \frac{k_1^2 - k_2^2}{k_1^2 + k_2^2}\right.$$
$$\left.\times\left(\frac{\partial^2}{\partial x\partial y}4\pi g_I\right)\right]P_x, \quad\quad (A7b)$$

$$E_z^{(x)} = -C\left[\frac{x}{\rho}I_\rho^V + \frac{k_1^2 - k_2^2}{k_1^2 + k_2^2}\left(\frac{\partial^2}{\partial x\partial z}4\pi g_I\right)\right]P_x; \quad\quad (A7c)$$

P_y dipole,

$$E_x^{(y)} = C\left[\frac{xy}{\rho^2}(I_\rho^H + I_\phi^H)\right.$$
$$\left. - \frac{k_1^2 - k_2^2}{k_1^2 + k_2^2}\left(\frac{\partial^2}{\partial x\partial y}4\pi g_I\right)\right]P_y, \quad\quad (A7d)$$

$$E_y^{(y)} = C\left\{\left[\left[\left(\frac{y}{\rho}\right)^2 I_\rho^H - \left(\frac{x}{\rho}\right)^2 I_\phi^H\right] - \frac{k_1^2 - k_2^2}{k_1^2 + k_2^2}\right.\right.$$
$$\left.\left.\times\left[\left(\frac{\partial^2}{\partial y^2} + k_2^2\right)4\pi g_I\right]\right\}P_y, \quad\quad (A7e)$$

$$E_z^{(y)} = -C\left[\frac{y}{\rho}I_\rho^V + \frac{k_1^2 - k_2^2}{k_1^2 + k_2^2}\left(\frac{\partial^2}{\partial y\partial z}4\pi g_I\right)\right]P_y; \quad\quad (A7f)$$

P_z dipole,

$$E_x^{(z)} = C\left[\frac{x}{\rho}I_\rho^V + \frac{k_1^2 - k_2^2}{k_1^2 + k_2^2}\left(\frac{\partial^2}{\partial x\partial z}4\pi g_I\right)\right]P_z, \quad\quad (A7g)$$

$$E_y^{(z)} = C\left[\frac{y}{\rho}I_\rho^V + \frac{k_1^2 - k_2^2}{k_1^2 + k_2^2}\left(\frac{\partial^2}{\partial y\partial z}4\pi g_I\right)\right]P_z, \quad\quad (A7h)$$

where

$$\hat{r}_{I,ij,x} = \frac{r_{I,ij,x}}{r_{I,ij}}, \quad\quad \hat{r}_{I,ij,y} = \frac{r_{I,ij,y}}{r_{I,ij}}, \quad\quad \hat{r}_{I,ij,z} = \frac{r_{I,ij,z}}{r_{I,ij}}, \quad\quad (A9a)$$

$$\beta_{I,ij} = [1 - (k_0 r_{I,ij})^{-2} + i(k_0 r_{I,ij})^{-1}], \quad\quad (A9b)$$

$$\gamma_{I,ij} = -[1 - 3(k_0 r_{I,ij})^{-2} + 3(k_0 r_{I,ij})^{-1}i], \quad\quad (A9c)$$

$$r_{I,ij} = |r_i - \bar{I}_R \cdot r_j| = [(x_i - x_j)^2 + (y_i - y_j)^2$$
$$+ (z_i + z_j)^2]^{1/2}. \quad\quad (A9d)$$

ACKNOWLEDGMENTS

REFERENCES

1. P. A. Bobbert and J. Vlieger, "Light scattering by a sphere on a substrate," Physica A **137**, 213–214 (1986).
2. F. L. Assi, "Electromagnetic wave scattering by a sphere on a layered substrate," M. S. thesis (University of Arizona, Tucson, Ariz., 1990).
3. I. V. Lindell, A. H. Sihvola, K. O. Muinonen, and P. W. Barber, "Scattering by a small object close to an interface. I. Exact-image theory formulation," J. Opt. Soc. Am. A **8**, 472–476 (1991).
4. B. R. Johnson, "Light scattering from a spherical particle on a conducting plane: I. Normal incidence," J. Opt. Soc. Am. A **9**, 1341–1351 (1992).
5. G. L. Wojcik, D. K. Vaughn, and L. K. Galbraith, "Calculation of light scatter from structures on silicon surfaces," in *Lasers in Microlithography*, J. S. Batchelder, D. J. Erlich, and J. Y. Tsao, eds., Proc. SPIE **774**, 21–31 (1987).
6. M. L. Liswith, "Numerical modeling of light scattering by individual submicron spherical particles on optically

smooth semiconductor surfaces," M. S. thesis (Arizona State University, Tempe, Ariz., 1994).

7. Y. A. Yeremin, N. V. Orlov, and A. G. Sveshnikov, "The analysis of complex diffraction problems by the discrete-source method," Comp. Math. Phys. **35**, 731–743 (1995).

8. E. M. Purcell and C. R. Pennypacker, "Scattering and absorption of light by nonspherical dielectric grains," Astrophys. J. **186**, 705–714 (1973).

9. B. T. Draine, "The discrete-dipole approximation and its application to interstellar graphite grains," Astrophys. J. **333**, 848–872 (1988).

10. B. T. Draine and P. J. Flatau, "The discrete-dipole approximation for scattering calculations," J. Opt. Soc. Am. A **11**, 1491–1499 (1994).

11. M. A. Taubenblatt and T. K. Tran, "Calculation of light scattering from particles and structure by the coupled-dipole method," J. Opt. Soc. Am. A **10**, 912–919 (1993).

12. A. Lakhtakia, "Macroscopic theory of the coupled dipole approximation method," Opt. Commun. **72**, 1–5 (1990).

13. A. Lakhtakia, "General theory of the Purcell–Pennypacker scattering approach and its extension to bianisotropic scatterers," Astrophys. J. **394**, 494–499 (1992).

14. J. I. Hage and J. M. Greenberg, "A model for the optical properties of porous grains," Astrophys. J. **361**, 251–259 (1990).

15. A. G. Hoekstra and P. M. A. Sloot, "Dipolar unit size in coupled-dipole calculations of the scattering matrix elements," Opt. Lett. **18**, 1211–1213 (1993).

16. J. W. Cooley and J. W. Tukey, "An algorithm for the machine calculation of complex Fourier series," Math. Comput. **19**, 297–301 (1965).

17. J. J. Talmonti, R. B. Kay, and D. J. Krebs, "Numerical model estimating the capabilities and limitations of the fast Fourier transform technique in absolute interferometry," Appl. Opt. **35**, 2182–2191 (1996).

18. B. Ritchie and M. D. Feit, "Fast Fourier transform computational method for the propagation of electromagnetic pulses through layered dielectric media," Phys. Rev. E **53**, 1976–1981 (1996).

19. F. Depasse and P. Groussel, "Use of two-dimensional fast Fourier transform in harmonic modulated thermal diffusion," Int. J. Heat Mass Transfer. **39**, 3761–3764 (1996).

20. J. J. Goodman, B. T. Draine, and P. J. Flatau, "Application of fast-Fourier-transform techniques to the discrete-dipole approximation," Opt. Lett. **16**, 1198–1200 (1991).

21. B. T. Draine and J. Goodman, "Beyond Clausius–Mossotti: wave propagation on a polarizable point lattice and the discrete dipole approximation," Astrophys. J. **405**, 685–697 (1993).

22. R. Schmehl, "The coupled-dipole method for light scattering for light particles on plane surfaces," M. S. thesis (Arizona State University, Tempe, Ariz., and the Institut für Thermische Strömungsmaschinen, Universität Karlsruhe, Karlsruhe, Germany, 1994).

23. D. L. Lager and R. J. Lytle, *FORTRAN Subroutines for the Numerical Evaluation of Sommerfeld Integrals unter Anterem*, Rep. UCRL-51821 (Lawrence Livermore Laboratory, Livermore, Calif., 1975).

24. M. Petravic and G. Kuo-Petravic, "An ILUCG algorithm which minimizes in the Euclidean norm," J. Comput. Phys. **32**, 263–269 (1979).

25. N. M. Brenner, "Fast Fourier transform of externally stored data," IEEE Trans. Audio Electroacoust. **AU-17**, 128–132 (1969).

26. C. F. Bohren and D. R. Huffman, *Absorption and Scattering of Light by Small Particles* (Wiley, New York, 1983).

27. B. M. Nebeker, G. W. Starr, and E. D. Hirleman, "Modeling of light scattering from structures with particle contaminants," in *Flatness, Roughness, and Discrete Defect Characterization for Computer Disks, Wafers, and Flat Panel Displays*, John Stover, eds., Proc. SPIE **2862**, 139–150 (1996).

28. H. C. Chen, *Theory of Electromagnetic Waves—A Coordinate-Free Approach* (McGraw-Hill, New York, 1983).